Combustion and Flame 294 (2026) 115350

Contents lists available at ScienceDirect

Combustion and Flame

journal homepage: www.sciencedirect.com/journal/combustion-and-flame

Numerical study on local characteristics of turbulent hydrogen/air flames at ambient and cryogenic temperatures

Linlin Yang [a,*], Yiqing Wang [b], Xiaohang Fang [a,c], Martin Davy [a], Felix Leach [a]

[a] Department of Engineering Science, University of Oxford, Oxford, OX1 3PJ, UK
[b] Department of Aeronautical and Aviation Engineering, The Hong Kong Polytechnic University, Hong Kong, 999077, China
[c] Department of Mechanical & Manufacturing Engineering, Schulich School of Engineering, University of Calgary, Calgary, T2L 1Y6, Canada

ARTICLE INFO

Keywords:
Hydrogen combustion
Cryogenic flame
Reacting flows
Direct numerical simulation
Turbulent flames

ABSTRACT

Hydrogen is a promising carbon-free fuel for achieving net zero. However, cryogenic conditions used for hydrogen storage introduce additional combustion safety concerns. Understanding the behavior of turbulent hydrogen/air flames under such conditions is therefore essential. In this study, three-dimensional direct numerical simulations (DNS) are conducted to investigate the local characteristics of turbulent stoichiometric hydrogen/air flames at ambient (300 K) and cryogenic (100 K) temperatures. The results show that cryogenic temperature suppresses small-scale flame wrinkling, leading to a smoother flame front and weaker flame acceleration than in the ambient case. This behavior is attributed to the increased curvature Markstein number at lower temperatures, which enhances the sensitivity of flame stretch to negative curvature and promotes the local destruction of flame surface area in highly curved regions. Both consumption and displacement speeds are negatively correlated with curvature, with the larger Markstein number arising from the greater gas expansion ratio under cryogenic conditions. In addition, both flames are thickened in a similar manner, as the large positive normal strain rate in the cryogenic flame is offset by negative kinematic restoration, resulting in a similar effective normal strain rate to that of the ambient flame. However, a narrower distribution of normalized surface density function indicates that turbulence has a weaker influence on the flame structure at cryogenic temperature. Moreover, due to reduced suppression of a key elementary reaction, the decorrelation between heat release rate (HRR) and fuel consumption rate (FCR) is more pronounced at cryogenic temperature. Furthermore, statistical analyses show that turbulence primarily affects reactions and mixing in the low-temperature zone, and its influence becomes weaker at lower initial temperature. This study provides new insights into turbulent hydrogen/air flames under cryogenic conditions and contributes to the prevention of combustion hazards during liquid hydrogen storage.

Novelty and Significance Statement

The novelty of this work lies in it providing the first detailed analysis of the local characteristics of turbulent hydrogen/air flames under ambient and cryogenic conditions. The study systematically quantifies how cryogenic temperature alters flame response to turbulence, identifies mechanisms governing the distinct flame morphology under cryogenic conditions, and clarifies the origin of flame thickening and its differences from the ambient flame. Additionally, it reveals how turbulence modifies chemistry and mixing in cryogenic flames, particularly in the low-temperature zone. This study fills a critical gap in the understanding of turbulent hydrogen/air flames under cryogenic conditions by revealing their local dynamics, structure, and chemistry. The findings are significant to hydrogen safety, as they provide the physical basis needed to mitigate combustion hazards associated with liquid hydrogen storage. The results are especially valuable for hydrogen combustion in cryogenic systems, where novel insights different from ambient-temperature scenarios are detailed.

* Corresponding author.
E-mail address: linlin.yang@eng.ox.ac.uk (L. Yang).

https://doi.org/10.1016/j.combustflame.2026.115350
Received 14 April 2026; Received in revised form 29 September 2026; Accepted 30 September 2026
Available online 8 October 2026
0010-2180/© 2026 The Authors. Published by Elsevier Inc. on behalf of The Combustion Institute. This is an open access article under the CC BY license (http://creativecommons.org/licenses/by/4.0/).

1. Introduction

Hydrogen is a promising carbon-free energy vector on the pathway to achieving net zero emissions [1]. However, the volumetric energy density of gaseous hydrogen is low [2]. Cryogenic conditions are commonly used to increase its energy density through storage as a liquid. Since hydrogen is highly diffusive and reactive, if there is a leak, hydrogen can mix with ambient air rapidly, forming cryogenic mixtures which can be easily ignited accidentally [3]. The resulting flame can be significantly accelerated by intrinsic instabilities such as the Darrieus–Landau instability (DLI) and thermo-diffusive instability (TDI) as well as by turbulence [4–6]. Sometimes deflagration-to-detonation transition (DDT) occurs, causing serious explosions [7,8]. Under cryogenic conditions, flame instabilities are much stronger and the run-up distance of DDT is much shorter than at ambient conditions [9]. Therefore, fires and explosions related to cryogenic hydrogen can be much more dangerous than those under ambient conditions. To prevent and mitigate potential hydrogen combustion hazards, it is necessary to understand hydrogen/air flame propagation under cryogenic conditions.

In the literature, there are several studies investigating cryogenic hydrogen/air flames in the laminar regime, where intrinsic flame instabilities play an important role in flame front wrinkling and acceleration. The minimum ignition energy of cryogenic hydrogen/air flames was experimentally studied Ghosh et al. [10]. The results showed that under cryogenic conditions, the minimum ignition energy increases, indicating that the reactivity is suppressed by the low temperature of the mixture. On the other hand, this low initial temperature leads to a large gas expansion ratio (the density ratio of unburnt to burnt gas, $\sigma = \rho_u/\rho_b$) across the cryogenic flame front, making the role of intrinsic instabilities, particularly the DLI, important for flame propagation and acceleration [4,5,11]. The effects of cryogenic temperature on laminar flame evolution have been studied in recent years under various configurations, such as closed channels [6,9,12], periodic channels [13], open space [14], and conical or Bunsen-like flames [15,16]. Pronounced flame wrinkling and significant acceleration were observed, even for stoichiometric hydrogen/air flames with negligible TDI. Enhanced DLI and flame front wrinkling caused by cryogenic temperature were highlighted in these studies. For fuel-lean hydrogen/air flames in which TDI plays an dominant role in cellular flame evolution, cryogenic temperatures also promote TDI [13,17]. Therefore, a cryogenic temperature affects flame propagation through enhanced intrinsic instabilities in the laminar regime. Considering that most combustion safety-relevant scenarios happens on a large scale where the existence of turbulence is inevitable, the effects of turbulence on cryogenic hydrogen combustion should also be examined.

Under turbulent conditions, previous studies on hydrogen/air flames have mainly focused on fuel-lean mixtures under ambient or high-pressure conditions. The effects of Karlovitz number (Ka, ratio of flame time scale to the Kolmogorov time scale) on fuel-lean hydrogen/air flame were investigated by Aspden et al. [18–21] using DNS. Their results showed that the TDI associated with the low Lewis number can significantly affect the flame regimes and the local chemical reactions. Various fuels such as hydrogen, methane, and propane were compared to examine the Lewis number effect, demonstrating that the unique characteristics of hydrogen flame [22,23]. Owing to the high diffusivity of hydrogen, a pronounced decorrelation of fuel consumption rate (FCR) and heat release rate (HRR) was observed [24]. Further chemical analysis showed that this decorrelation is caused by the diffusion of atomic hydrogen in the low-temperature (preheat) zone [25]. The interaction between flame instabilities and turbulence in fuel-lean hydrogen/air flames was also studied by Lee et al. [26] and Lipatnikov et al. [27] using DNS with detailed chemistry, where the roles of molecular diffusion and turbulent intensity were examined in detail. Temperature and turbulence intensity effects on the global flame acceleration and local flame dynamics of fuel-lean hydrogen/air flame under engine-relevant conditions were examined by Wang et al. [28,29]. However, discussions on the impact of cryogenic initial temperature, which is vital to safety issues of liquid hydrogen storage, on hydrogen/air flame's response to turbulence were scarce. A relevant study by Chen et al. [30] showed that under cryogenic conditions, the flame tends to form large-scale but smooth wrinkles, resulting in significant flame acceleration. The impact of enhanced DLI on flame evolution at cryogenic conditions was highlighted. Nevertheless, local flame characteristics under cryogenic conditions are not fully understood in the literature. Furthermore, turbulence–flame interaction is more relevant to Ka [31], however, differences in flame response to turbulence at ambient and cryogenic temperatures for fixed Ka remain largely unclear. This motivates the present work, which investigates the flame response to turbulence at ambient and cryogenic temperatures.

In this study, local characteristics of turbulent stoichiometric hydrogen/air flame at ambient and cryogenic temperatures are studied through three-dimensional direct numerical simulations considering detailed chemical kinetics. The objective is to examine the behaviors of turbulent hydrogen/air flames with fixed Ka and Damköhler number (Da) at cryogenic ($T_0 = 100$ K) and ambient ($T_0 = 300$ K) temperatures. Effects of turbulence on local dynamics, structure, and chemistry of ambient and cryogenic flames are discussed.

This paper is laid out as follows. First, the numerical configuration for three-dimensional DNS is introduced in Section 2. Then, in Section 3, overall flame behavior, global flame propagation, and local flame characteristics are discussed. Finally, the main findings of this study are summarized.

2. Numerical setup

The DNS simulations presented in this work are based on the low-Mach number formulation for reactive flows. The governing equations describing momentum transport and conservation of species and enthalpy in low Mach number reactive flows are given by [19]

$$\frac{\partial(\rho \boldsymbol{u})}{\partial t} + \nabla \cdot (\rho \boldsymbol{u}\boldsymbol{u}) = -\nabla \pi + \nabla \cdot \boldsymbol{\tau} + \rho \boldsymbol{F} \tag{1}$$

$$\frac{\partial(\rho Y_i)}{\partial t} + \nabla \cdot (\rho Y_i \boldsymbol{u}) = \nabla \cdot (\rho D_i \nabla Y_i) + \rho \omega_i \tag{2}$$

$$\frac{\partial(\rho h)}{\partial t} + \nabla \cdot (\rho h \boldsymbol{u}) = \nabla \cdot (\lambda \nabla T) + \sum_i \nabla \cdot (\rho h_i D_i \nabla Y_i) \tag{3}$$

where ρ is the density, $\boldsymbol{u}$ is the velocity, $\boldsymbol{F}$ is the momentum source (an external forcing term used to sustain turbulence), τ is the stress tensor, h is the specific enthalpy of the gas mixture, T is the temperature, λ is the thermal conductivity, and Y_i, D_i, ω_i, and h_i are the mass fraction, mixture-averaged diffusion coefficients, net production rate, and enthalpy of species i, respectively. The total pressure p is decomposed into the sum of a spatially constant thermodynamic pressure P_0 and a perturbation pressure that drives the flow, π, i.e., $p = P_0 + \pi$.

The equation set is supplemented by the ideal-gas equation of state

$$P_0 = \rho R_{mix} T = \rho \mathscr{R} \sum_i \frac{Y_i}{W_i} \tag{4}$$

where W_i is the molecular weight of species i, $\mathscr{R}$ is the universal gas constant. The relationship between enthalpy, species and temperature is given by

$$h = \sum_i Y_i h_i(T) \tag{5}$$

Downward-propagating turbulent flames using the canonical 'flame-in-a-box' configuration are modeled [19]. A high-aspect ratio domain (1:1:8) with periodic lateral boundary conditions is employed, with outflow at the top and a free-slip solid at the base, as shown in Fig. 1. Since this study focuses on local flame characteristics, a small domain with a width of $L_x = L_y = 4l_F$ is used. Here, laminar flame thickness is defined as $l_F = (T_b - T_0)/(dT/dx)_{max}$, where T_0, T_b and $(dT/dx)_{max}$ are

Table 1
Parameters for turbulent hydrogen/air flames at $\phi = 1$ and $P_0 = 1$ atm.

Case	100 K	300 K
Expansion ratio, $\sigma = \rho_u/\rho_b$	19.3	6.82
Laminar flame speed, S_L [m/s]	0.56	2.36
Laminar flame thickness, l_F [mm]	0.266	0.363
Domain width, L_x, [mm]	1.06	1.45
Domain length, L_z, [mm]	8.50	11.61
Turbulence intensity, u'/S_L	3	3
Reynold number, Re	66.7	47.5
Taylor microscale Reynold number, Re_λ	31.6	26.7
Karlovitz number, Ka	8.22	8.22
Damköhler number, Da	0.13	0.13

unburnt and burnt gas temperature, and the maxima of temperature gradient of a corresponding one-dimensional adiabatic, unstretched, planar flame (1D laminar flame). The domain height is $L_z = 8L_x$. A 1D laminar flame is also used for the initiation of corresponding turbulent flame. To establish turbulence, an inert simulation is run and the turbulent velocity field is superimposed onto the 1D free flame profile. The turbulence is maintained by adding a source term in the momentum equation [32]. The source term, $\boldsymbol{F}$, introduces a long-wavelength forcing that injects kinetic energy into low-wavenumber modes to sustain statistically stationary homogeneous isotropic turbulence while allowing the inertial cascade to develop naturally. This term leads to an integral length $l_t \approx L_x/10 = 0.4l_F$ [19]. Note that the domain size used in this study is relatively small and domain size-independent results for global flame speed is not obtained. However, local characteristics and chemistry that are not sensitive to domain size are focus of this work [20,23,33].

This study investigates turbulent flames in stoichiometric hydrogen/air mixtures (equivalence ratio $\phi = 1$) at ambient pressure ($P_0 = 1$ atm). Two initial temperatures are considered, $T_0 = 100$ K (cryogenic) and 300 K (ambient). The relevant parameters for simulation setup are listed in Table 1. The expressions for the calculation of the Karlovitz number, Ka, Damköhler number, Da, and Reynold numbers based on l_t and Taylor microscale $\lambda = u'(15\nu/\epsilon)^{1/2}$ are [19]

$$Ka^2 = \frac{u'^3}{S_L^3}\frac{l_F}{l_t},\quad Da = \frac{S_L}{u'}\frac{l_t}{l_F} \tag{6}$$

$$Re = \frac{u' l_t}{\nu},\quad Re_\lambda = \frac{u'\lambda}{\nu} \tag{7}$$

where u' is the turbulent rms velocity fluctuation, S_L is the 1D laminar flame speed, $\epsilon = u'^3/l_t$ is the dissipation rate, and ν is the kinematic viscosity in the unburnt mixture.

Aspden et al. [31] showed that the Ka is more relevant to the interaction between turbulence and the flame front. To isolate the effect of the cryogenic temperature (100 K), turbulent fluctuation velocity $u'/S_L = 3$, $Ka = 8.2$, and $Da = 0.13$, are fixed for both temperatures in this study. In the turbulence regime diagram, both cases are in the thin reaction zone [34].

PeleLMeX is used for the 3D DNS with detailed chemistry and transport model [35,36]. The Navier–Stokes equations for incompressible reactive flows are solved with second-order in time and space. This low-Mach number solver as well as the 'flame-in-a-box' configuration has been validated in previous DNS of hydrogen, methane, and dodecane flames over a wide range of equivalence ratio and Ka number [20,22,31,37]. A detailed chemical mechanism [38] is used and the mixture-averaged transport model is considered in the simulation. The ideal gas equation of state is used since the non-ideal gas effect is not pronounced for cryogenic flames at ambient pressure [6,16]. Adaptive mesh refinement (AMR) is employed in the simulations. The refinement criteria are based on flame features (HO_2 concentration) and are therefore independent of the forcing. In addition, a wide buffer region is imposed ahead of the flame front at each AMR level to ensure that the turbulence has sufficient time to cascade to the finer scales. Therefore, the AMR does not interact with the forcing and does not affect the turbulence–flame interactions. In each case, the simulation is initially run without refinement to reduce the computational cost of reaching a steady state. Refinement is then applied, and statistical data are collected after $15\tau_e$ ($\tau_e = l_t/u'$ is the eddy turnover time). Two levels of AMR are used, leading to an effective resolution of $128 \times 128 \times 1024$. There are 32 grid points within a laminar flame thickness and the criterion $\Delta x = \Delta y = \Delta z < 2\eta_k$ is satisfied (where η_k is the Kolmogorov length scale) [39]. Therefore, both flame front and turbulence can be well-resolved in the simulations.

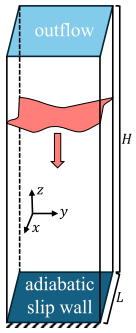


Fig. 1. Schematic of the flame-in-a-box configuration. The flame propagates downward.

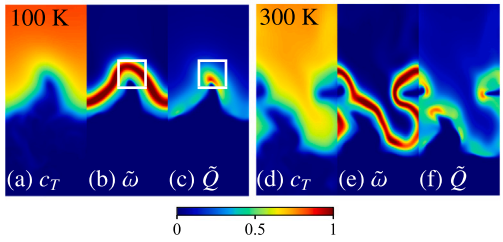


Fig. 2. Representative 2D slices of normalized temperature, fuel consumption rate and heat release rate of three-dimensional simulations for cryogenic (a–c) and ambient (d–f) hydrogen/air flames. The same color ranges are used for $T_0 = 100$ K and 300 K. The flame propagates from the top to the bottom.

3. Results and discussion

3.1. Overview of general flame behavior

To show the basic flame structure and influence of the cryogenic condition, two-dimensional slices of temperature, fuel (H_2) consumption rate (FCR) $\dot{\omega}_{H_2}$, and heat release rate (HRR) are presented in Fig. 2. For clarity, all values are normalized by the laminar values (1D unstretched laminar flames):

$$c_T = \frac{T - T_0}{T_b - T_0},\quad \tilde{\omega} = \frac{\dot{\omega}(H_2)}{\dot{\omega}^{1D}_{max}(H_2)},\quad \tilde{Q} = \frac{HRR}{2HRR^{1D}_{max}} \tag{8}$$

For the cryogenic case at $T_0 = 100$ K, a flame front wrinkled by turbulence is observed. From Fig. 2(a), it is clear that the unburnt gas right ahead of the flame front is disturbed by turbulent mixing, resulting in several regions with higher temperature than T_0. The interaction between turbulence and the flame results in a deep cusp towards the burnt gas, highlighted by the white box in Figs. 2(b) and (c). Near the cusp, the normalized HRR is pronounced. It is found that the region with high $\tilde{Q}$ is different from that with high $\tilde{\omega}$. This decorrelation is commonly observed in fuel-lean hydrogen/air flame where TDI is significant [25]. The mechanism of this phenomenon in a stoichiometric mixture will be discussed later.

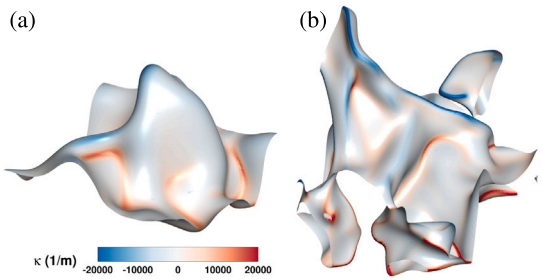


Fig. 3. Flame surfaces colored by mean curvature for (a) $T_0 = 100$ K and (b) $T_0 = 300$ K. The flame propagates downward.

For $T_0 = 300$ K, flame front wrinkling is more pronounced than for $T_0 = 100$ K, as shown in Fig. 2(d–f). The reaction front is highly wrinkled, and low-temperature unburnt gas penetrates into the hot burnt gas. It is also clear that the distributions of FCR and HRR on the flame front are not uniform. The non-uniformity is more pronounced for the normalized HRR shown in Fig. 2(f). This feature is similar to the cryogenic case ($T_0 = 100$ K). As the effective Lewis number for stoichiometric hydrogen/air is slightly larger than 1, a negative correlation between FCR and the flame curvature is expected. For both cases shown in Fig. 2, the most intensely burning regions are observed at the cusps of the flame front with large negative curvature.

To examine the role of curvature on flame morphology, the distribution of curvature on the flame front is shown in Fig. 3. The flame front is extracted based on the iso-surface of the water mass fraction, $Y(H_2O)$, corresponding to the location of peak heat release rate (HRR) in a one-dimensional laminar flame profile. The corresponding progress variable, defined based on $Y(H_2O)$ as $c = Y(H_2O)/Y^{1D}_{max}(H_2O)$, takes values of 0.171 and 0.147 for $T_0 = 100$ K and 300 K, respectively. It is evident that the flame front is greatly wrinkled, forming cusps with large negative curvature. Compared to the cryogenic flame, the flame front for $T_0 = 300$ K is more corrugated, with small structures superimposed on the large cusp. These small structures exhibit very large curvature. Wrinkles with various length scales can be observed in Fig. 3(b), demonstrating stronger influence of turbulence on the ambient flame at $T_0 = 300$ K. For $T_0 = 100$ K, only large-scale wrinkles are observed while the flame front remains smooth. This result is consistent with previous work by Chen et al. [30]. Since wrinkled flame surface greatly affects the global flame propagation, it is expected that the propagation speed for $T_0 = 300$ K will be much faster.

3.2. Global flame acceleration

To aid the analysis of local flame characteristics, the global acceleration of turbulent flames is first examined. Turbulent flame propagation is quantified using the global consumption speed S_T [40]:

$$S_T = \frac{-1}{\rho_u(Y_{H_2,u} - Y_{H_2,b})A_0} \int \dot{\omega}_{H_2} \mathrm{dxdy} \tag{9}$$

where $\dot{\omega}_{H_2}$ is the net consumption rate of H_2, A_0 is the cross section, ρ and Y_{H_2} are density and H_2 mass fraction, with subscripts 'u' and 'b' denoting the unburnt and burnt states, respectively. The global consumption speed is affected by two factors: (1) flame surface area increase related to flame wrinkling, A/A_0; (2) stretch factor due to local reaction enhancement, I. Therefore:

$$\frac{S_T}{S_L} = \frac{A}{A_0} \cdot I \tag{10}$$

To determine the flame surface area, generalized flame surface density, $\Sigma = |\nabla c_T|$ is calculated. Similar to Wang et al. [41], a progress variable based on temperature, c_T, is used:

$$A = \int \Sigma dV = \int |\nabla c_T| dV \tag{11}$$

Table 2
Time-averaged values of S_T/S_L, A/A_0, and I for turbulent hydrogen/air flames at $\phi = 1$.

Initial temperature	100 K	300 K
S_T/S_L	1.22	2.37
A/A_0	1.46	2.74
I	0.84	0.86

For turbulent flames at $T_0 = 100$ K and 300 K, the mean values of S_T/S_L, A/A_0, and I are listed in Table 2. The increase in flame surface area A/A_0 is larger than 1, indicating that turbulence can accelerate flame propagation through flame front wrinkling. The result that A/A_0 is larger at $T_0 = 300$ K is consistent with the contours shown in Figs. 2 and 3, where flame front wrinkling is more significant for $T_0 = 300$ K.

On the other hand, the values of stretch factor I are 0.84 and 0.86 for $T_0 = 100$ K and $T_0 = 300$ K, respectively. These values are smaller than 1, indicating that local reactions are suppressed when turbulence is imposed. In previous studies [14] on laminar flames, the TDI is considered negligible since the effective Lewis number of the stoichiometric hydrogen/air mixture is close to 1 (slightly larger than 1). In this work, the turbulent intensity is higher ($u'/S_L = 3$) and it is found that the stretch factor may play a noticeable role in flame acceleration.

Note that the values of A/A_0 and I may change with the domain size, as mentioned in Hunt and Aspden [23]. However, in this study we use these parameters to quantify effects of turbulence on local flame characteristics rather than to achieve a general conclusion for flame acceleration over a wide range of domain sizes.

3.3. Local flame dynamics

To explain the role of turbulence in local flame behavior, local flame speed including displacement speed (S_d) and consumption speed (S_c) as well as flame stretch rate and its components are calculated and averaged over time [4,11]. These local parameters are calculated throughout the computational domain and subsequently extracted on the selected iso-surface of the progress variable. The displacement speed is calculated as [15,42]:

$$S_d = \frac{1}{|\nabla Y|}\frac{DY}{Dt} = \frac{1}{|\nabla Y|}\left(\frac{\partial Y}{\partial t} + \mathbf{u}\cdot\nabla Y\right) \tag{12}$$

where Y is the mass fraction of water, i.e., $Y(H_2O)$. DY/Dt denotes the substantial derivative of Y. Using the species transport equation, S_d can be rewritten as:

$$S_d = \frac{1}{\rho|\nabla Y|}\mathbf{n}\cdot\nabla(\rho D|\nabla Y|) - D\nabla\cdot\mathbf{n} + \frac{\omega}{\rho|\nabla Y|} \tag{13}$$

where $\mathbf{n}$ is the flame normal vector and D is species diffusivity. To take into account the thermal expansion effect across the flame front, density-weighted flame displacement speed, $S_d^* = \rho S_d/\rho_u$ is commonly used. The normal vector $\mathbf{n}$ is calculated as:

$$\mathbf{n} = -\frac{\nabla Y}{|\nabla Y|} \tag{14}$$

Mean flame curvature can be calculated through:

$$\kappa = \frac{1}{2}\nabla\cdot\mathbf{n} \tag{15}$$

The stretch rate K is defined as the fractional rate of change of a flame surface element δA [11]:

$$K = \frac{1}{\delta A}\frac{\delta A}{dt} \tag{16}$$

Both tangential strain rate a_t and curvature stretch $K_c = S_d\nabla\cdot\mathbf{n}$ contribute to the flame stretch:

$$K = a_t + S_d\nabla\cdot\mathbf{n} = a_t + K_c \tag{17}$$

The tangential strain rate a_t and normal strain rate a_n are related to the divergence of the velocity $\mathbf{u}$, i.e., the dilatation, $\nabla \cdot \mathbf{u}$ [43]:

$$a_t = \nabla \cdot \mathbf{u} - a_n = \nabla \cdot \mathbf{u} - \mathbf{nn} : \nabla \mathbf{u} \tag{18}$$

The calculation of local consumption speed follows the approach in the literature [44–46]. Tubes normal to the iso-surface are constructed and consumption-based local speed is calculated through integration of fuel consumption rate in each tube with a volume Ω_i and surface area A_i. The integration tubes follow the gradient of the progress variable and extend into both the burned and unburned mixtures over a distance of $3l_F$ on each side of the iso-surface. This integration length ensures that the entire reaction zone is included in the calculation and that the results are insensitive to the choice of integration length. Because the cross-sectional area of each tube varies only slightly along the normal direction of the iso-surface, the average cross-sectional area is close to that at the iso-surface. Consequently, the consumption-based speed used in this work provides a practical approximation to the conventional definition of the consumption speed [11]. It effectively quantifies the local reaction enhancement and has been widely used in previous studies [23,44,45]. The local consumption speed can be expressed as [46]:

$$S_c = \frac{-1}{\rho_u(\mathrm{Y_{H_2,u}} - \mathrm{Y_{H_2,b}})\mathrm{A_i}} \int_{\Omega_i} \rho \dot{\omega}_{\mathrm{H_2}} \mathrm{d}\Omega_\mathrm{i} \tag{19}$$

The joint probability density functions (JPDFs) and marginal PDFs of normalized hydrogen consumption rate and curvature are shown in Fig. 4. Note that the local parameters are calculated on the iso-surface of $\mathrm{Y(H_2)}$ corresponding to the HRR peak in the one-dimensional laminar flame profile [45]. In both cases, there is a negative correlation between local consumption rate and the flame curvature. This is a feature for mixtures with Lewis numbers larger than 1. Due to the stretch–chemistry interaction [47], reactions are pronounced in regions with negative curvature. To evaluate the dependence of S_c on κ, linear fits are superimposed on the JPDFs, as indicated by the dashed lines in Fig. 4. Quantitatively, the slopes obtained from least squares regression for $T_0 = 100$ K and $T_0 = 300$ K are −0.54 and −0.36, respectively, indicating that the cryogenic flame is more sensitive to the curvature change. It is also clear that flame segments that are positively curved exhibit a smaller local consumption speed than the one-dimensional unstretched flame speed. However, in the negatively curved region, the local consumption speed can be much larger than S_L, demonstrating enhanced chemical reactions in the flame cusps.

The width of normalized curvature distribution is indicative of the variance in flame curvature. In Fig. 4, it is evident that the normalized curvature variance for $T_0 = 100$ K is smaller than that for $T_0 = 300$ K. Narrower curvature distribution around $\kappa = 0$ indicates that the local flame surface is relative smooth and only large-scale wrinkles appear. This statistical result also agrees well with the observation shown in Fig. 2 where weaker large-scale flame front wrinkling is observed for $T_0 = 100$ K.

To evaluate the interaction between turbulence and the flame front, JPDFs of normalized flame displacement speed and local curvature along with their marginal PDFs are shown in Fig. 5. A negative correlation can be observed for both cases. This is also characteristic of a flame with $Le > 1$. Quantitatively, the slopes for T_0 =100 K and 300 K are −0.35 and −0.24, respectively. Therefore, under cryogenic conditions ($T_0 = 100$ K), S_d^*/S_L exhibits greater sensitivity to local curvature variations. This trend is similar to the results of consumption speed shown in Fig. 4.

Theoretically, two curvature Markstein numbers, $\mathcal{M}^d$ and $\mathcal{M}^c$, can be introduced to quantify the sensitivities of displacement and consumption speeds to curvature, respectively [11,48,49].

$$S_c^*/S_L = 1 - \mathcal{M}^c \cdot \kappa l_F \tag{20}$$

$$S_d^*/S_L = 1 - \mathcal{M}^d \cdot \kappa l_F \tag{21}$$

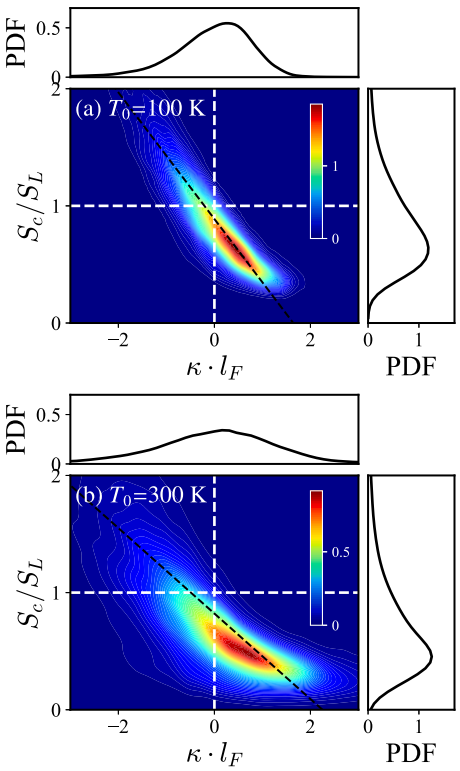


Fig. 4. JPDFs of normalized consumption speed and curvature for (a) T_0 = 100 K and (b) T_0 = 300 K. The dashed lines show the linear fitting results.

For stoichiometric hydrogen/air mixtures, the effective Lewis number is slightly greater than unity. The larger expansion ratio at T_0 = 100 K leads to higher curvature Markstein numbers [48,49]. This analytical prediction is in qualitative agreement with the numerical results shown in Figs. 4 and 5. Therefore, cryogenic conditions result in a higher expansion ratio and, consequently, larger curvature Markstein numbers, leading to a more pronounced sensitivity of local flame speeds to curvature. Note that both flame speeds are functions of curvature and strain rate. Introducing an additional strain term could further improve these equations. However, the present work focuses primarily on the effect of curvature. The influence of strain rate on cryogenic flame dynamics and modeling will be investigated in future work.

The correlation between displacement speed and total flame stretch, along with their marginal PDFs is shown in Fig. 6. For the ambient flame at $T_0 = 300$ K, most flame segments exhibit positive stretch and thereby smaller density-weighted displacement speed than the corresponding laminar flame speed ($Kl_F/S_L > 0, S_d^*/S_L < 1$). A similar phenomenon can be observed at $T_0 = 100$ K. A clear difference between two flames is in the $Kl_F/S_L \approx 0$ region. Several segments of the flame front exhibit near-zero or even negative S_d^*/S_L for $T_0 = 300$ K.

The JPDFs of normalized density-weighted flame stretch and curvature are shown in Fig. 7. From a theoretical point of view, flame stretch rate is defined as the fractional rate of change of a flame surface element [4,11]. Therefore, positive flame stretch is relevant to the generation of flame surface area. On the other hand, negative flame curvature tends to destroy the flame surface [50,51]. For both cases, flame stretch is large when the curvature is close to zero, indicating that the flame surface is generated in the regions that are relatively smooth. In contrast, the stretch rate decreases and becomes negative when the absolute curvature is large, whether positive or negative. This indicates that the flame surface is destroyed in regions that are significantly curved.

The initial temperature T_0 shows a great impact on the correlation between stretch and curvature. At $T_0 = 100$ K, the normalized flame

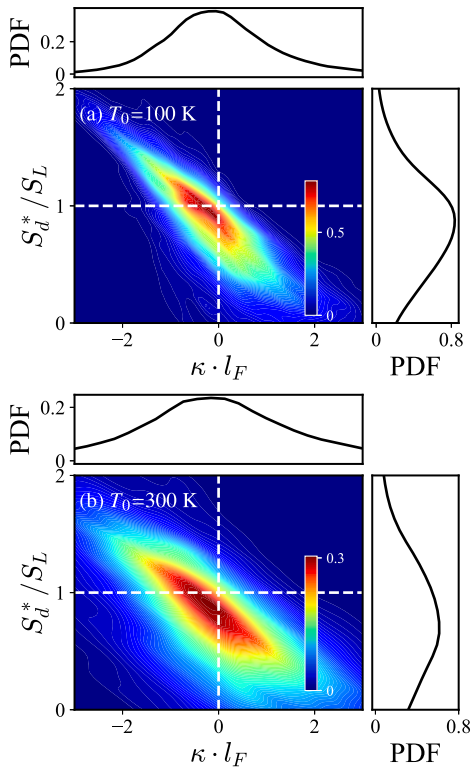


Fig. 5. JPDFs of normalized displacement speed and curvature for (a) T_0 = 100 K and (b) T_0 = 300 K.

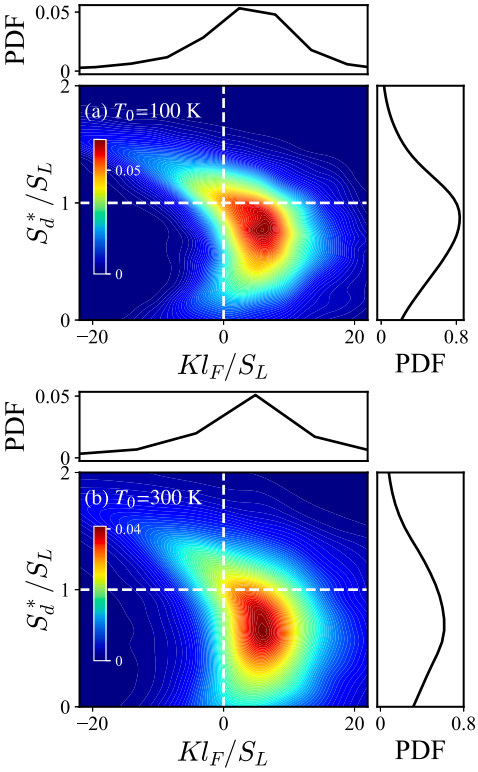


Fig. 6. JPDFs of normalized displacement speed and stretch rate for (a) T_0 = 100 K and (b) T_0 = 300 K.

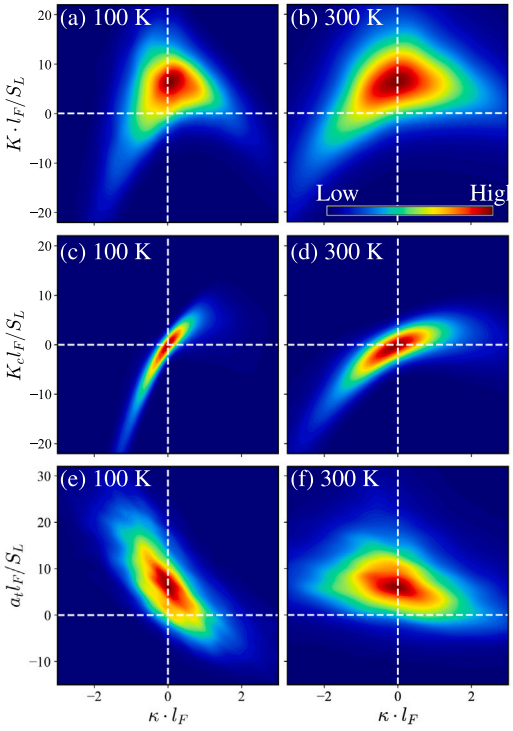


Fig. 7. JPDFs of (a, b): normalized stretch rate, (c, d) normalized curvature stretch, and (e, f) normalized tangential strain rate versus normalized curvature for T_0 = 100 K and T_0 = 300 K.

stretch decreases sharply when the negative curvature decreases, while it decreases moderately when positive curvature increases, as shown in Fig. 7(a). This results in an obvious asymmetric feature for the cryogenic flame, which is distinct from that in Fig. 7(b) for T_0 = 300 K where the stretch decreases slowly as the negative curvature decreases. This explains why the flame front wrinkling at T_0 = 100 K is relatively weak compared to T_0 = 300 K: the cryogenic flame surface is quickly destroyed in the negatively curved region. This high sensitivity of stretch rate to negative curvature greatly suppresses the small-scale wrinkling of the cryogenic flame front and leads to a relatively smooth front.

According to Eq. (17), both the tangential strain rate, a_t, and the curvature stretch, K_c, contribute to the total stretch rate. To examine the origin of the higher sensitivity of the stretch rate to curvature at T_0 = 100 K, Figs. 7(c–f) show the JPDFs of the normalized a_t and K_c with curvature [52,53]. It is observed that the contributions of a_t and K_c to K depend strongly on curvature. In regions of large positive curvature, K_c is positive while a_t is negative; the large magnitude of a_t leads to negative K and the annihilation of flame surface area. In negatively curved regions, their roles are reversed. Additionally, in the region where $\kappa \cdot l_F < 0$, the rapid decrease of K_c with decreasing curvature is responsible for the high sensitivity of the stretch rate to curvature shown in Fig. 7(a). Considering that $K_c = 2S_d \cdot \kappa$, this high sensitivity originates from the greater sensitivity of the normalized density-weighted displacement speed to curvature at T_0 = 100 K, as shown in Fig. 5. Therefore, the relatively smooth and weakly wrinkled flame front observed for T_0 = 100 K is attributed to the strong sensitivity of the displacement speed to curvature.

3.4. Flame thickening

Apart from wrinkling the flame front, the presence of turbulence can alter the local thickness of the flame front. To quantify the role of turbulence in flame thickening, statistical analysis on the surface

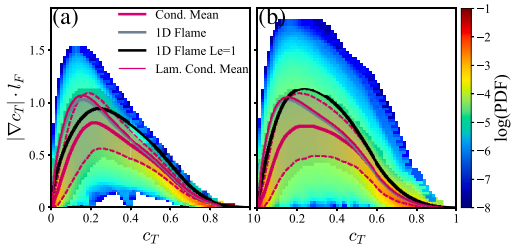


Fig. 8. JPDFs of normalized surface density function and c_T for (a) $T_0 = 100$ K and (b) $T_0 = 300$ K. The dashed lines and shaded area indicate the standard deviation.

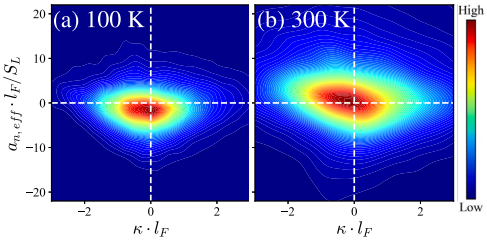


Fig. 9. JPDFs of normalized effective normal strain rate and curvature for (a) $T_0 = 100$ K and (b) $T_0 = 300$ K.

density function, $|\nabla c_T|$ is performed. The value of $|\nabla c_T|$ is relevant to the reciprocal of flame thickness. Fig. 8 displays the JPDFs of $|\nabla c_T|$ and c_T. For better comparison, the conditional mean and profiles of a 1D flame with/without unity Lewis number transport model and the corresponding 3D laminar flame (with the same configuration and domain size as the turbulent case, but without imposed turbulence) are normalized and shown in the figure. Compared to the ambient flame shown in Fig. 8(b), the JPDF for $T_0 = 100$ K becomes narrower. This indicates the effect of turbulence on cryogenic flame thinning or thickening is weaker. In addition, local thinning of the cryogenic flame is observed in the region $|\nabla c_T| \cdot l_F > 1$. However, only a small portion of the cryogenic flame is thinned, compared to the ambient flame with broaden JPDF distribution. These statistical features also demonstrate that the cryogenic flame is less affected by turbulence.

It is readily seen that the conditional means of $|\nabla c_T|$ on c_T is lower than the 1D flame profile, demonstrating that the overall flame is thickened when turbulence is imposed. For both flames, thickening is pronounced when $c_T < 0.5$. While in the high temperature zone when $c_T > 0.5$, the conditional mean is very close to the profile of the 1D laminar flame, which is the same for both flames. Moreover, the shape of the turbulent flame profile and its peak location closely match those of the 1D laminar flame with unity Lewis number transport model. This implies that turbulence plays an important role in flame thickening and its influence does not have noticeable or qualitative change when the initial temperature of unburnt mixture decreases. Furthermore, the profiles of the 3D laminar flames are very close to those of the corresponding 1D laminar flames, suggesting that turbulence, rather than DLI, is the dominant mechanism responsible for flame thickening and thinning.

As listed in Table 1, the expansion ratio at $T_0 = 100$ K is much larger than that at $T_0 = 300$ K. This indicates a higher dilatation at lower T_0. According to Eq. (18) and the results of a_t in Fig. 7(e–f), it is expected that the normal strain rate for case $T_0 = 100$ K will be much larger than that for case $T_0 = 300$ K. As positive normal strain rate tend to decrease $|\nabla c_T|$, the thickening of the cryogenic flame should be more pronounced. To explain this observation in Fig. 8, the balance equation for $|\nabla c|$ is analyzed [42,54,55]:

$$\frac{1}{|\nabla c|}\frac{d|\nabla c|}{dt} = -(a_n + \mathbf{n}\cdot\nabla S_d) = -a_{n,eff} \tag{22}$$

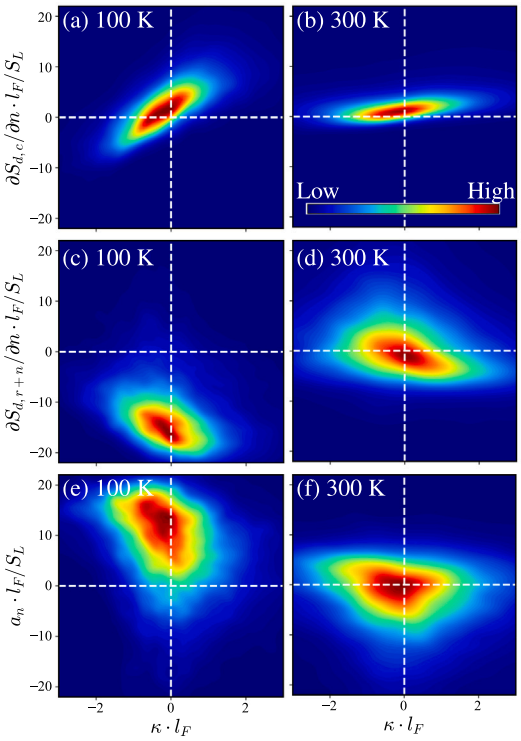


Fig. 10. JPDFs of components of normalized $a_{n,eff}$ and curvature for (a) $T_0 = 100$ K and (b) $T_0 = 300$ K.

where $a_{n,eff}$ is the effective normal strain rate. The displacement speed can be decomposed into its normal diffusion $S_{d,n}$, curvature $S_{d,c}$, and reaction components $S_{d,r}$, therefore:

$$\frac{1}{|\nabla c|}\frac{d|\nabla c|}{dt} = -(a_n + \partial S_{d,r+n}/\partial n + \partial S_{d,c}/\partial n) \tag{23}$$

where $\partial S_{d,r+n}/\partial n$ and $\partial S_{d,c}/\partial n$ are the kinematic restoration and curvature terms, respectively. Positive value of $a_{n,eff}$ results in a smaller value of $|\nabla c|$ and thereby flame thickening.

Fig. 9 displays the JPDFs of normalized $a_{n,eff}$ and curvature. It is seen that the JPDF for case $T_0 = 100$ K is more concentrated. However, there is no qualitative difference between two flames. This agrees well with the results shown in Fig. 8. Larger dilatation for $T_0 = 100$ K does not change local flame thickening greatly.

To explain this, the JPDFs of the components of $a_{n,eff}$ and curvature are presented in Fig. 10. It is found from Figs. 10(a) and (b) that the curvature terms are relative small for both flames, particularly for the ambient flame at $T_0 = 300$ K. The cryogenic condition primarily affects the kinematic restoration term and the normal strain rate. Compared to case $T_0 = 300$ K, the kinematic restoration term for $T_0 = 100$ K is much smaller while the normal strain rate is larger. This demonstrates that, although larger a_n for tend to reduce $|\nabla c|$, its influence is largely counteracted by the smaller kinematic restoration term. Consequently, their combined effects on $|\nabla c|$ do not have qualitative differences between $T_0 = 100$ K and $T_0 = 300$ K.

The change in local flame speed and thickness affects the local values of Ka. As Ka is highly relevant to the turbulence–flame interaction, it is important to examine the statistics of local Karlovitz number, Ka_{loc}. Here, Ka_{loc} is calculated based on the local consumption speed and local flame thickness. The PDF of the ratio of Ka_{loc} to the global Ka is presented in Fig. 11. It is found that the distribution of Ka_{loc}/Ka for $T_0 = 300$ K peaks around $Ka_{loc} = Ka$, suggesting that most flame segments experience turbulence–flame interactions governed by the global Karlovitz number.

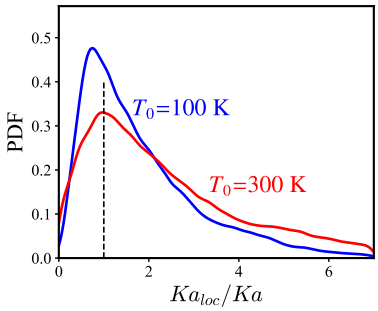


Fig. 11. PDF of normalized local Karlovitz number for T_0 = 100 K and 300 K. The dashed line denotes $Ka_{loc}/Ka = 1$.

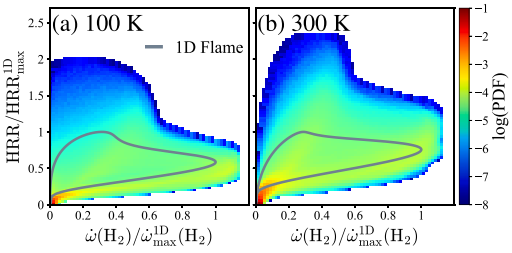


Fig. 12. JPDFs of normalized FCR and HRR for (a) T_0 = 100 K and (b) T_0 = 300 K.

Compared to T_0 = 100 K, the PDF of Ka_{loc}/Ka for T_0 = 300 K shows a pronounced tail ($Ka_{loc}/Ka > 3$). This tail indicates that more segments of the ambient flame experience much larger local Ka_{loc} than its global value. Therefore, turbulence–flame interaction for T_0 = 300 K can be much stronger in some regions of the flame front. This result also supports the observation in Fig. 2.

3.5. Turbulence–chemistry interaction

One interesting observation from Fig. 2 is the decorrelation between heat release rate (HRR) and fuel consumption rate (FCR). As shown in the white box in Figs. 2(b) and (c), the HRR peaks in the region with large negative curvature. However, the FCR is relatively low in that region. This phenomenon has also been observed in fuel-lean turbulent hydrogen/air flames [24]. To investigate this phenomenon under cryogenic conditions, JPDFs of normalized FCR and HRR are shown in Fig. 12. Both FCR and HRR are normalized by corresponding maxima in 1D laminar flame profiles.

In both cases, the conditional mean of HRR (see red lines) peaks at a moderate fuel consumption rate, i.e., $\dot{\omega}(H_2)/\dot{\omega}^{1D}_{max}(H_2) \approx 0.3$. However, compared to T_0 = 300 K, there are considerable flame segments showing high HRR at very low fuel consumption rates ($\dot{\omega}(H_2)/\dot{\omega}^{1D}_{max}(H_2)$ <0.2) for T_0 = 100 K. This indicates that decorrelation between HRR and FCR is more pronounced at cryogenic temperatures. This phenomenon is quite counter-intuitive, as high HRR is related to intense chemical reactions, which is greatly suppressed under the cryogenic temperature of the mixture.

To explain the pronounced HRR at relatively low FCR, we first examine the JPDFs of normalized HRR and c_T shown in Fig. 13. To better display the role of turbulence on chemical heat release, the HRR profiles of 1D unstretched laminar flame with and without unity Lewis number transport model are also shown in Fig. 13. It is evident that the conditional mean of normalized HRR for both flames shows significant discrepancy from the corresponding 1D unstretched laminar profile, suggesting that turbulence has great effect on HRR as well as the chemical reactions. Additionally, it is found that c_T corresponding

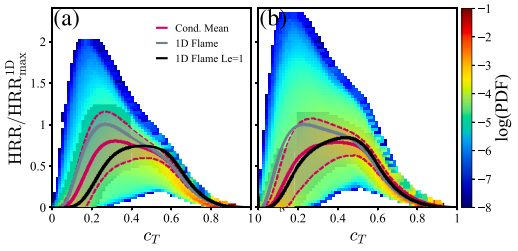


Fig. 13. JPDFs of normalized HRR and c_T for (a) T_0 = 100 K and (b) T_0 = 300 K. The dashed lines and shaded area indicate the standard deviation.

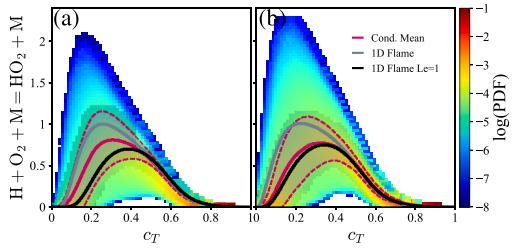


Fig. 14. JPDFs of normalized reaction rate and c_T for (a) T_0 = 100 K and (b) T_0 = 300 K. The dashed lines and shaded area indicate the standard deviation.

to the peak of HRR shifts to a high value, demonstrating that significant heat release occurs in higher temperature if turbulence exists. Since turbulence can enhance mixing process in preheat zone, the delayed HRR peak in temperature space is associated with turbulence-enhanced transport of reactant to the high temperature regions of the flame.

Another observation in Fig. 13 is that the HRR profile for both flame approaches the profile of the 1D unstretched flame with Le = 1. This can be explained using the effective Lewis number [34,56]:

$$Le_{eff,T} = \frac{\alpha + D_T}{D_i + D_T} \tag{24}$$

where α and D_i are thermal and mass diffusivity of the mixture and species i, respectively, and D_T is the turbulent diffusivity which accounts for the effect of turbulence on species transport through increased mixing. This D_T can be assumed to be equal for all of scalars (species and temperature) as turbulence is expected to mix all scalars the same way. If the turbulence is intense enough, the dominant effect of transport is D_T, resulting in $Le_{eff,T} = 1$. This explains why the HRR profile approaches the 1D flame profile with Le = 1. Moreover, it is readily seen that the ambient flame is more close to the 1D laminar flame with Le = 1, further suggesting that the cryogenic flame is less affected by turbulent mixing.

A distinct difference between T_0 = 100 K and T_0 = 300 K is the fluctuation of HRR around c_T = 0.5. As shown in Fig. 13, the HRR fluctuation can be quantified through the standard deviation denoted by the pink region. For T_0 = 100 K, the fluctuation around c_T = 0.3 is the most significant. At c_T = 0.5, the fluctuation is less obvious. This demonstrates that for T_0 = 100 K, the turbulence mainly affects the preheat zone, while the reaction zone is less affected by the turbulence. In contrast, for T_0 = 300 K, the fluctuation of HRR is pronounced over a wide range of c_T, indicating that the turbulence has stronger influence on the chemical structure of the ambient flame.

Aspden et al. [25] showed that the reaction in the low-temperature zone is mainly attributed to the atomic hydrogen (H). The dominant elementary reaction responsible for this decorrelation is H+O_2+M=> HO_2+M. The role of this reaction is also mentioned in previous studies of weakly turbulent flames [57,58]. To examine whether this still holds for the stoichiometric mixture under cryogenic conditions, the JPDFs of the rate of this reaction and c_T are presented in Fig. 14. It is clear

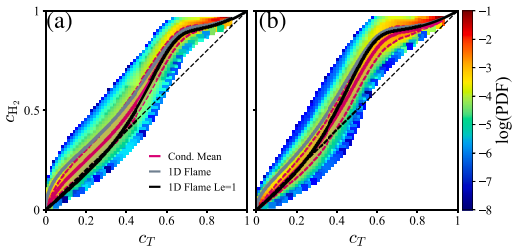


Fig. 15. JPDFs of progress variables based on temperature c_T and fuel mass fraction c_{H_2} for (a) T_0 = 100 K and (b) T_0 = 300 K. The dashed lines and shaded area indicate the standard deviation.

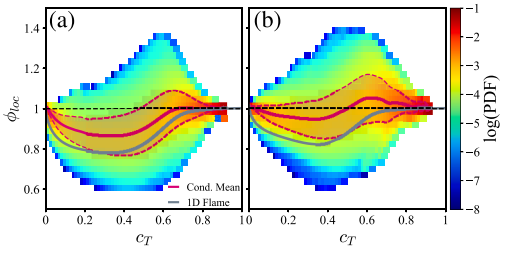


Fig. 16. JPDFs of local equivalence ratio ϕ_{loc} and c_T for (a) T_0 = 100 K and (b) T_0 = 300 K. The dashed lines and shaded area indicate the standard deviation.

that the JPDFs are similar to those of HRR and c_T shown in Fig. 13, demonstrating the high relevance of this reaction to HRR. In the low-temperature zone, this reaction rate is suppressed by turbulence for both flames. However, the cryogenic flame shown in Fig. 14(a) is less affected than the ambient flame shown in Fig. 14(b), which results in higher HRR at lower FCR, i.e., the decorrelation of FCR and HRR.

In addition, for T_0 = 100 K the profiles of 1D flames with and without Le = 1 effectively encompass the conditional mean of this reaction rate, while for T_0 = 300 K, the conditional mean almost collapses onto the profile of 1D flames with Le = 1. This further demonstrates that the chemical structure of the cryogenic flame is less affected by the turbulence than the ambient flame.

As explained above, for the stoichiometric hydrogen/air flame, turbulence significantly affects reactions in the low-temperature zone under different T_0. To quantify the effects of turbulence mixing, JPDFs of progress variables based on temperature c_T and fuel mass fraction c_{H_2} are shown in Fig. 15. The results show that at a given c_T, the value of c_{H_2} is consistently smaller than that of the 1D unstretched flame. This demonstrates that turbulence enhances mixing processes in the low-temperature zone and facilitates the transport of H_2 fuel to regions of higher temperature.

An obvious observation is that, for T_0 = 300 K, c_T and c_{H_2} collapse onto each other. This means that the progress variables measured by temperature and fuel mass fraction are the same, which is a characteristics of a unity Lewis number mixture. This shows that the low-temperature zone of the ambient flame is perfectly mixed by the turbulence.

Turbulent mixing by turbulence is also reflected on the distribution of local equivalence ratio. JPDFs of local equivalence ratio and c_T are displayed in Fig. 16. The local equivalence ratio is defined as $\phi_{loc} = X_H/2X_O$, where X_H and X_O are molar fractions of H and O atoms, respectively. Compared to T_0 = 100 K, the local equivalence ratio at T_0 = 300 K is close to its initial value, 1. This shows that effects of turbulence at T_0 = 300 K is more significant and plays a dominant role over molecular diffusion. This again agrees well with previous analysis. Note that the relatively low Karlovitz number (Ka) considered in this study can limit the impact of turbulent mixing compared with that in high-Ka turbulent flames. Nevertheless, the shift of the conditional mean profiles towards the unity Lewis number profiles in Figs. 13–16 suggests that turbulent mixing still plays a role in the local flame characteristics. As shown in the previous sections, the flame dynamics are primarily governed by curvature and stretch. This is expected because the turbulence considered in this work is relatively weak.

In summary, turbulence greatly affects chemical reactions of the stoichiometric hydrogen/air flames in the low-temperature zone. For the cryogenic flame, the phenomenon that high heat release rate occurs in regions with relatively low fuel consumption rate is more pronounced, which is related to higher reaction rate of $H+O_2+M=>HO_2+M$. In addition, the cryogenic flame is less affected by turbulent mixing in the low-temperature zone.

4. Conclusions

In this study, local characteristics of turbulent stoichiometric hydrogen/air flames at ambient (T_0 =300 K) and cryogenic (T_0 =100 K) temperatures are investigated using three-dimensional DNS with detailed chemistry and a mixture-averaged transport model. Both the Karlovitz and the Damköhler numbers are fixed to isolate the effects of temperature on local characteristics of turbulent flames in the thin reaction regime.

The results show that the flame morphologies at ambient and cryogenic temperatures are markedly different. The cryogenic temperature significantly inhibits small-scale flame front wrinkling, leading to a smoother flame surface than the ambient flame. The cryogenic flame exhibits smaller absolute curvature, whereas small-scale wrinkles with large curvature are more prevalent in the ambient case. Analyses show that this behavior is linked to the larger curvature Markstein number arising from the greater gas expansion ratio at lower initial temperatures. The resulting higher sensitivity of flame stretch to negative curvature promotes local destruction of flame surface area in highly curved regions, thereby inhibiting small-scale wrinkle formation and maintaining a smoother flame front. Local flame dynamics analyses also show that both normalized displacement and consumption speeds are negatively correlated with curvature, with greater sensitivity at lower initial temperatures.

Flame thickening is observed for both flames and the thickening level does not change qualitatively with initial temperature. Detailed analyses show that, for the cryogenic flame, negative kinematic restoration counteracts the positive normal strain rate, resulting in little difference in the effective normal strain rate compared with the ambient flame. However, the JPDF of the surface density function becomes narrower in the cryogenic flame, demonstrating that turbulence has a weaker influence on flame thickness. Moreover, turbulence–flame interaction is less pronounced at cryogenic conditions and the local Karlovitz number is distributed around its global value. For the ambient flame, an obvious tail at large local Karlovitz number is observed.

The chemical reactions in the low-temperature zone are greatly affected by the turbulence, resulting in a shift of conditional means towards the profiles of the unity-Lewis number flames. However, high heat release rates can occur in regions with low fuel consumption rates, and this decorrelation is more pronounced at cryogenic temperature. The elementary reaction in the low-temperature zone, $H+O_2+M=>HO_2+M$, which is less suppressed by turbulence at lower initial temperature, is closely related to this phenomenon. Moreover, turbulent mixing significantly affects fuel transport and the local equivalence ratio in the ambient flame, whereas its influence on the cryogenic flame is weaker.

The present work considers relatively weak turbulence (Ka = 8.2) and focuses on local turbulence–flame interaction under cryogenic conditions. Previous studies [19,59,60] showed that the global flame behavior can be quite different under strong turbulence. Additionally, a larger computational domain is necessary to fully capture the global flame propagation and the evolution of large structures. Future work will extend the analysis to higher Reynolds and Karlovitz numbers and larger computational domains to assess the observed cryogenic effects under stronger turbulence relevant to practical hydrogen release scenarios.

CRediT authorship contribution statement

Linlin Yang: Writing – original draft, Visualization, Methodology, Investigation, Formal analysis, Conceptualization. **Yiqing Wang:** Writing – review & editing, Formal analysis, Conceptualization. **Xiaohang Fang:** Writing – review & editing, Formal analysis. **Martin Davy:** Writing – review & editing, Funding acquisition. **Felix Leach:** Writing – review & editing, Supervision, Formal analysis.

Declaration of competing interest

The authors declare that they have no known competing financial interests or personal relationships that could have appeared to influence the work reported in this paper.

Acknowledgments

This study is funded by the Engineering and Physical Sciences Research Council Prosperity Partnership (EPSRC, Grant No. EP/T005327/1) and the John Fell Oxford University Press Research Fund, UK (0016719). Dr. Yang acknowledges the Advanced Research Computing (ARC) at Oxford for providing HPC resources.

References

[1] P.E. Lapenna, L. Berger, F. Creta, H. Pitsch, Hydrogen laminar flames, in: E.-A. Tingas (Ed.), Hydrogen for Future Thermal Engines, Springer International Publishing, Cham, 2023, pp. 93–139, Series Title, Green Energy and Technology.
[2] K. Senecal, F. Leach, Racing Toward Zero: The Untold Story of Driving Green, SAE International, 2021.
[3] D. Yu, Z. Chen, Premixed flame ignition: Theoretical development, Prog. Energy Combust. Sci. 104 (2024) 101174.
[4] C.K. Law, Combustion Physics, Cambridge University Press, Cambridge, 2006.
[5] M.A. Liberman, Combustion Physics: Flames, Detonations, Explosions, Astrophysical Combustion and Inertial Confinement Fusion, Springer International Publishing, Cham, 2021.
[6] L. Yang, Z. Chen, Effects of cryogenic temperature on premixed hydrogen/air flame propagation in a closed channel, Proc. Combust. Inst. 39 (2023) 2991–2999.
[7] E.S. Oran, Understanding explosions – from catastrophic accidents to creation of the universe, Proc. Combust. Inst. 35 (2015) 1–35.
[8] E.S. Oran, V.N. Gamezo, Origins of the deflagration-to-detonation transition in gas-phase combustion, Combust. Flame 148 (2007) 4–47.
[9] M. Kuznetsov, A. Denkevits, A. Veser, A. Friedrich, Flame propagation regimes and critical conditions for flame acceleration and detonation transition for hydrogen-air mixtures at cryogenic temperatures, Int. J. Hydrog. Energy 47 (2022) 30743–30756.
[10] A. Ghosh, N. Munoz-Munoz, D. Lacoste, Minimum ignition energy of hydrogen-air and methane-air mixtures at temperatures as low as 200 K, Int. J. Hydrog. Energy 47 (2022) 30653–30659.
[11] T. Poinsot, D. Veynante, Theoretical and Numerical Combustion, R.T Edwards, 2005.
[12] X. Shen, W. Fu, W. Liang, J. Wen, H. Liu, C. Law, Strong flame acceleration and detonation limit of hydrogen-oxygen mixture at cryogenic temperature, Proc. Combust. Inst. 39 (2023) 2967–2977.
[13] L. Yang, T. Zhang, Y. Wang, X. Fang, F. Leach, Z. Chen, Non-linear evolution and acceleration of unstable fuel-lean hydrogen/air flame at ambient and cryogenic temperatures, Combust. Flame 280 (2025) 114346.
[14] L. Yang, Y. Wang, Z. Chen, Propagation and self-acceleration of circular expanding hydrogen/air flames at cryogenic temperature, Combust. Flame 265 (2024) 113501.
[15] L. Yang, Y. Wang, T. Zirwes, F. Zhang, H. Bockhorn, Z. Chen, Effects of intrinsic instabilities on the response of premixed hydrogen/air conical flames to inlet flow perturbations, Flow Turbul. Combust. 112 (2024) 1275–1297.
[16] S.L. Michaux, K.P. Chatelain, W.L. Roberts, D.A. Lacoste, Laminar burning velocities of hydrogen-air and methane-air flames from ambient to cryogenic temperatures at different equivalence ratios, Int. J. Hydrog. Energy 100 (2025) 608–616.
[17] L. Berger, A. Attili, H. Pitsch, Intrinsic instabilities in premixed hydrogen flames: Parametric variation of pressure, equivalence ratio, and temperature. Part 1 - Dispersion relations in the linear regime, Combust. Flame 240 (2022) 111935.
[18] A. Aspden, M. Day, J. Bell, Characterization of low Lewis number flames, Proc. Combust. Inst. 33 (2011) 1463–1471.
[19] A. Aspden, M. Day, J. Bell, Turbulence–flame interactions in lean premixed hydrogen: transition to the distributed burning regime, J. Fluid Mech. 680 (2011) 287–320.
[20] A. Aspden, M. Day, J. Bell, Towards the distributed burning regime in turbulent premixed flames, J. Fluid Mech. 871 (2019) 1–21.
[21] A. Aspden, T. Howarth, E. Hunt, Three-dimensional phenomenology of freely-propagating thermodiffusively-unstable lean premixed hydrogen flames, Proc. Combust. Inst. 40 (2024) 105634.
[22] A. Aspden, M. Day, J. Bell, Lewis number effects in distributed flames, Proc. Combust. Inst. 33 (2011) 1473–1480.
[23] E. Hunt, A. Aspden, Thermodiffusively-unstable lean premixed hydrogen flames: Length scale effects and turbulent burning regimes, Combust. Flame 272 (2025) 113855.
[24] A. Aspden, M. Day, J. Bell, Turbulence-chemistry interaction in lean premixed hydrogen combustion, Proc. Combust. Inst. 35 (2015) 1321–1329.
[25] A. Aspden, A numerical study of diffusive effects in turbulent lean premixed hydrogen flames, Proc. Combust. Inst. 36 (2017) 1997–2004.
[26] H. Lee, P. Dai, M. Wan, A. Lipatnikov, Displacement speed, flame surface density and burning rate in highly turbulent premixed flames characterized by low Lewis numbers, J. Fluid Mech. 961 (2023) A21.
[27] A.N. Lipatnikov, H. Lee, P. Dai, M. Wan, V.A. Sabelnikov, Transition from turbulence-dominated to instability-dominated combustion regime in lean hydrogen-air flames, Combust. Flame 259 (2024) 113170.
[28] Y. Wang, C. Xu, C. Chi, Y. Yang, Z. Chen, Temperature effect on turbulent burning velocity of lean premixed hydrogen/air flames, Phys. Fluids 36 (2024) 125165.
[29] Y. Wang, C. Xu, R. Scarcelli, Turbulent burning velocity of lean premixed hydrogen/air flames at engine conditions: Effects of turbulence intensity and length scale, Combust. Flame 282 (2025) 114504.
[30] C. Chen, C. Chi, D. Thévenin, W. Han, L. Yang, Effects of cryogenic temperature on turbulent premixed hydrogen/air flames, Proc. Combust. Inst. 40 (2024) 105749.
[31] A. Aspden, M. Day, J. Bell, Three-dimensional direct numerical simulation of turbulent lean premixed methane combustion with detailed kinetics, Combust. Flame 166 (2016) 266–283.
[32] A. Aspden, N. Nikiforakis, S. Dalziel, J. Bell, Analysis of implicit LES methods, Commun. Appl. Math. Comput. Sci. 3 (2008) 103–126.
[33] A.R. Varma, U. Ahmed, N. Chakraborty, Turbulence Effects on the Statistical Behaviour and Modelling of Flame Surface Density and the Terms of Its Transport Equation in Turbulent Premixed Flames, Flow Turbul. Combust. 111 (2023) 531–565.
[34] N. Peters, Turbulent combustion, in: Cambridge Monographs on Mechanics, Cambridge University Press, 2000.
[35] L. Esclapez, M. Day, J. Bell, A. Felden, C. Gilet, R. Grout, M. Henry de Frahan, E. Motheau, A. Nonaka, L. Owen, B. Perry, J. Rood, N. Wimer, W. Zhang, PeleLMeX: an AMR Low Mach Number Reactive Flow Simulation Code without level sub-cycling, J. Open Source Softw. 8 (2023) 5450.
[36] M.T. Henry de Frahan, L. Esclapez, J. Rood, N.T. Wimer, P. Mullowney, B.A. Perry, L. Owen, H. Sitaraman, S. Yellapantula, M. Hassanaly, M.J. Rahimi, M.J. Martin, O.A. Doronina, S.N. A., M. Rieth, W. Ge, R. Sankaran, A.S. Almgren, W. Zhang, J.B. Bell, R. Grout, M.S. Day, J.H. Chen, The pele simulation suite for reacting flows at exascale, in: Proceedings of the 2024 SIAM Conference on Parallel Processing for Scientific Computing, 2024, pp. 13–25.
[37] A. Aspden, J. Bell, M. Day, F. Egolfopoulos, Turbulence–flame interactions in lean premixed dodecane flames, Proc. Combust. Inst. 36 (2017) 2005–2016.
[38] Y. Zhang, W. Dong, L. Vandewalle, R. Xu, G. Smith, H. Wang, Foundational fuel chemistry model version 2.0 (FFCM-2), 2023, FFCM-2 Website. https://web.stanford.edu/group/haiwanglab/FFCM2.
[39] S.B. Pope, Turbulent flows, Meas. Sci. Technol. 12 (2001) 2020–2021.
[40] L. Berger, A. Attili, H. Pitsch, Intrinsic instabilities in premixed hydrogen flames: parametric variation of pressure, equivalence ratio, and temperature. Part 2 – non-linear regime and flame speed enhancement, Combust. Flame 240 (2022) 111936.
[41] Y. Wang, C. Xu, C. Chi, Z. Chen, Direct numerical simulations of turbulent premixed cool flames: Global and local flame dynamics analysis, Combust. Flame 270 (2024) 113759.
[42] H. Wang, E.R. Hawkes, J.H. Chen, B. Zhou, Z. Li, M. Aldén, Direct numerical simulations of a high karlovitz number laboratory premixed jet flame – an analysis of flame stretch and flame thickening, J. Fluid Mech. 815 (2017) 511–536.
[43] S.B. Pope, Turbulent Flows, Cambridge University Press, 2000.
[44] M. Day, J. Bell, P.-T. Bremer, V. Pascucci, V. Beckner, M. Lijewski, Turbulence effects on cellular burning structures in lean premixed hydrogen flames, Combust. Flame 156 (2009) 1035–1045.
[45] T. Howarth, A. Aspden, An empirical characteristic scaling model for freely-propagating lean premixed hydrogen flames, Combust. Flame 237 (2022) 111805.
[46] T. Howarth, E. Hunt, A. Aspden, Thermodiffusively-unstable lean premixed hydrogen flames: Phenomenology, empirical modelling, and thermal leading points, Combust. Flame 253 (2023) 112811.

[47] X. Chen, H. Böttler, A. Scholtissek, C. Hasse, Z. Chen, Effects of stretch-chemistry interaction on chemical pathways for strained and curved hydrogen/air premixed flames, Combust. Flame 232 (2021) 111532.
[48] M. Matalon, C. Cui, J.K. Bechtold, Hydrodynamic theory of premixed flames: effects of stoichiometry, variable transport coefficients and arbitrary reaction orders, J. Fluid Mech. 487 (2003) 179–210.
[49] J. Bechtold, M. Matalon, The dependence of the Markstein length on stoichiometry, Combust. Flame 127 (1) (2001) 1906–1913.
[50] S.M. Candel, T.J. Poinsot, Flame stretch and the balance equation for the flame area, Combust. Sci. Technol. 70 (1990) 1–15.
[51] H. Wang, E.R. Hawkes, J. Ren, G. Chen, K. Luo, J. Fan, 2-d and 3-D measurements of flame stretch and turbulence–flame interactions in turbulent premixed flames using DNS, J. Fluid Mech. 913 (2021) A11.
[52] H.F. Ahmed, D. Zhumabayeva, S. Trivedi, R.S. Cant, Stretch rate and displacement speed statistics for local flame topology in turbulent premixed flames, Flow Turbul. Combust. 115 (2025) 863–886.
[53] G. Ozel-Erol, M. Klein, N. Chakraborty, Lewis number effects on flame speed statistics in spherical turbulent premixed flames, Flow Turbul. Combust. 106 (2021) 1043–1063.
[54] R. Sankaran, E.R. Hawkes, J.H. Chen, T. Lu, C.K. Law, Structure of a spatially developing turbulent lean methane–air bunsen flame, Proc. Combust. Inst. 31 (2007) 1291–1298.
[55] C. Chi, B. Cuenot, D. Thévenin, Turbulent flame–wall interaction: dynamics of flame thickness and combustion regime, J. Fluid Mech. 1029 (2026) A5.
[56] B. Savard, B. Bobbitt, G. Blanquart, Structure of a high Karlovitz n-C7H16 premixed turbulent flame, Proc. Combust. Inst. 35 (2015) 1377–1384.
[57] J.B. Chen, H.G. Im, Stretch effects on the burning velocity of turbulent premixed hydrogen/air flames, Proc. Combust. Inst. 28 (2000) 211–218.
[58] H. Carlsson, R. Yu, X.-S. Bai, Flame structure analysis for categorization of lean premixed CH4/air and H2/air flames at high Karlovitz numbers: Direct numerical simulation studies, Proc. Combust. Inst. 35 (2015) 1425–1432.
[59] S. Luca, A. Attili, E. Lo Schiavo, F. Creta, F. Bisetti, On the statistics of flame stretch in turbulent premixed jet flames in the thin reaction zone regime at varying Reynolds number, Proc. Combust. Inst. 37 (2019) 2451–2459.
[60] A. Attili, S. Luca, D. Denker, F. Bisetti, H. Pitsch, Turbulent flame speed and reaction layer thickening in premixed jet flames at constant Karlovitz and increasing Reynolds numbers, Proc. Combust. Inst. 38 (2021) 2939–2947.